PROCEEDINGS OF SCIENCE

# The Multipolar Structure of the Local Expansion Rate

**Basheer Kalbouneh, Christian Marinoni* and Julien Bel**

*Aix Marseille Univ, Université de Toulon, CNRS, CPT, Marseille, France*
*E-mail:* basheer.kalbouneh@cpt.univ-mrs.fr,
christian.marinoni@cpt.univ-mrs.fr, julien.bel@cpt.univ-mrs.fr

We design a new observable, the $\eta$ expansion rate fluctuation, to characterize deviations from linearity in the redshift-distance relationship in the local Universe. We also show how to compress the resulting signal into spherical harmonic coefficients in order to better decipher the structure and symmetries of the anisotropies in the local expansion rate. We apply this analysis scheme to several public catalogs of redshift-independent distances, the Cosmicflows-3 and Pantheon data sets, covering the redshift range $0.01 < z < 0.05$.
The leading anisotropic signal is stored in the dipole. Within the standard cosmological model, it is interpreted as a bulk motion ($307 \pm 23$ km/s) of the entire local volume in a direction aligned at better than 4 degrees with the bulk component of the Local Group velocity with respect to the CMB. This term alone, however, provides an overly simplistic and inaccurate description of the angular anisotropies of the expansion rate. We find that the quadrupole contribution is non-negligible ($\sim 50\%$ of the anisotropic signal), in fact, statistically significant, and signaling a substantial shearing of gravity in the volume covered by the data. In addition, the 3D structure of the quadrupole is axisymmetric, with the expansion axis aligned along the axis of the dipole.
Implications of these findings for the determination of the Hubble constant $H_0$ are discussed.

*Corfu Summer Institute 2022 "School and Workshops on Elementary Particle Physics and Gravity",*
*28 August - 1 October, 2022*
*Corfu, Greece*

*Speaker





PoS(CORFU2022)239

## 1. Introduction

The lack of convergence to a consensus value for the Hubble constant has triggered a search for the reliability of non-standard cosmological line elements. The question is whether metrics with a lower degree of symmetry than FRW, while remaining simple, provide a reliable description of the data in regions below the uniformity scale [1].

We have addressed this problem in [2] by determining the multipole structure of the fluctuations in the expansion rate of the local patch of the universe. By exploiting a new observable, the expansion rate fluctuation $\eta$, we have shown that unexpected symmetries in the multipole components of the expansion rate field appear whether the analysis is performed on independent data such as galaxy or SNIa.

In the following, we highlight the main methodology developed to estimate the expansion rate fluctuation field from available catalogs of redshift-independent distances. We also review the main results obtained in [2]. We display formulas in natural units ($c = 1$) and we refer to the standard $\Lambda$CDM model, as the flat FRW spacetime which best fits the Planck18 data [3].

## 2. The Local Expansion Rate Fluctuations

An observable that captures deviations from the linear redshift-distance relation is the *expansion rate fluctuation* [2]

$$\eta \equiv \log \frac{z}{H_0 d_L}. \tag{1}$$

where $z$ is the redshift, $d_L$ is the luminosity distance, and $H_0$ is a normalizing factor whose amplitude is fixed by requiring that the average value of the fluctuations over the volume covered by data vanishes. As detailed in [2], a statistically unbiased estimator of the expansion rate fluctuations is

$$\hat{\eta} = \log \left[ \frac{z}{H_0} \right] + 5 - \frac{\mu}{5} \tag{2}$$

where $\mu$ is the distance modulus of a cosmic source. Since the latter quantity is normally distributed, it follows that $\hat{\eta}$ is also a Gaussian random variable (if we ignore the error in redshift) with an uncertainty $\delta$ reflecting the imprecision with which the redshift-independent distances are estimated ($\delta = \sigma_\mu/5$).

At each point in space-time, there are, among others, two characteristic observers of the large-scale structure of the universe: the *matter-comoving* observer, sharing the motion of the surrounding dust flow and b) the *CMB-comoving* observer, at rest in a reference frame in which the CMB dipole disappears. These observers are indistinguishable in a uniform universe described by the FRW metric. On the other hand, they provide different estimates of the redshift and distance of the same source in a space-time with arbitrary geometry

If one adopts the point of view of the matter-comoving observer, then, on very small scales, i.e. for redshifts smaller than a caracteristic scale $z_l << 1$ the expansion rate fluctuation $\eta$ becomes independent on redshift and simply converges to $\log(\mathfrak{H}_0/H_0)$, where $\mathfrak{H}_0$ is the effective Hubble parameter in a generic 4D spacetime, as defined by [4–6].

If, instead, one considers an observer who, in first approximation, sees an isotropic CMB, then $\eta$, which diverges when $z$ goes to zero, has a straightforward physical interpretation within a FLRW cosmological model: it is related to the radial component of the resulting peculiar velocity as

$$\hat{\eta} \approx \frac{v(1+z)}{z \ln 10}. \tag{3}$$

The versatile nature of the $\eta$ observable is thus evident. When evaluated by a matter-comoving observer, it provides insights into fluctuations of the spacetime metric in a fully unperturbative way, thus allowing investigations beyond the standard cosmological scenario in a model-independent way. This approach is pursued in [7]. If evaluated in the CMB rest frame, instead, as done by [2] and in this paper, $\eta$ sheds light on a standard cosmological observable and is thus instrumental in placing constraints on the perturbative sector of the FRW model.

## 3. The multipolar structure of the expansion rate fluctuation

We can compress the information contained in the $\eta$ observable into a few coefficients. To this end, we expand the expansion rate field $\eta$ in Spherical Harmonic (SH) components. We orthogonally decompose $\eta$ on a sphere as follows

$$\eta = \sum_{\ell=0}^{\infty} \sum_{m=-\ell}^{\ell} a_{\ell m} Y_{\ell m}(\theta, \phi) = \sum_{\ell=0}^{\infty} \eta_{\ell}, \tag{4}$$

where $Y_{\ell m}(\theta, \phi)$ is the spherical harmonic function. Thus, the Fourier coefficients $a_{\ell m}$ can be expressed as

$$a_{\ell m} \equiv \int_0^{2\pi} \int_0^{\pi} \eta(\theta, \phi) Y^*_{\ell m}(\theta, \phi) \sin\theta \, d\theta d\phi. \tag{5}$$

Note that, due to the definition, the monopole ($\ell = 0$) of $\eta$ vanishes. In addition, one can define the angular power spectrum of the $\eta$ anisotropy as

$$C_{\ell} = \langle |a_{\ell m}|^2 \rangle_e, \tag{6}$$

where the expectation is intended to be over a statistical ensemble of universes.

$$\hat{C}_{\ell} = \frac{1}{2\ell + 1} \sum_{m=-\ell}^{\ell} |a_{\ell m}|^2, \tag{7}$$

is an unbiased estimator for $C_{\ell}$.

### 3.1 Estimation of the angular $\eta$ field

The expansion rate fluctuation estimator $\hat{\eta}(\mathbf{r})$ is a discrete random variable. The analysis of this observable can be simplified, and the underlying continuous theoretical model (1) can be better traced if we convert it into a stochastic field. We thus average $\hat{\eta}(\mathbf{r})$ over all the objects at position $\mathbf{r}$ within a given volume $V(\Omega, R)$, where $\Omega$ is a solid angle centered on the observer and $R$ the

depth of the catalog (i.e. its upper edge). The angular anisotropies seen by the observer are thus piece-wise defined as

$$\eta(\Omega) = \frac{\sum_i^N \hat{\eta}(\mathbf{r}_i) w(\mathbf{r}_i) W(\mathbf{r}_i|V(\Omega, R))}{\sum_i^N w(\mathbf{r}_i) W(\mathbf{r}_i|V(\Omega, R))} \tag{8}$$

where $N$ is the number of objects in the catalog, $w(\mathbf{r}_i) = 1/\delta_i^2$ is a weight that takes into account the precision in the measurement of the distance of the *i-th* object in the catalog. $W(\mathbf{r}|V(\Omega, R))$ is a window function which evaluates to unity if $\mathbf{r}_i \in V$ and is null otherwise.

It is clear that averaging has the advantage of reducing noise at the cost of a lower angular resolution. The latter is essentially controlled by the aperture of the solid angle $\Omega$, although it also depends, in principle, on the depth $R$ of the sample on which the spatial averaging is performed.

In practice, we construct the $\eta$ 2D field out of a discrete point process $\hat{\eta}(\mathbf{r})$, by first partitioning the sky in $N_{pix}$ identical pixels (each subtending a solid angle $\Omega_i$) using HEALPix [8] and then by applying eq. (8) to objects within the volume $V$ subtended by each pixel $\Omega_i$. HEALPix is an algorithm which tessellates a spherical surface into curvilinear quadrilaterals, each covering the same area as every other. Although characterized by a different shape. The resolution of the HEALPix grid is calculated as $N_{pix} = 12N_{side}^2$ where $N_{side} = 2^t$, and $t \in \mathbb{N}$. The baseline grid, corresponding to $t = 0$, has 12 pixels. Once the value of $\eta$ is estimated in each pixel, the Fourier coefficients of the spherical harmonic decomposition are computed using HEALPix.

### 3.2 Estimation of Measurement Errors

We determine the errors, both statistical and systematic, that affect the SH reconstruction by means of Monte Carlo simulations. We consider as input model the Fourier coefficients (up to $\ell_{max} = 3N_{side} - 1$) measured from the data, and we use them to simulate a fiducial $\eta$ field. We then randomly perturb the expansion field, at the angular position of the objects, by means of a Gaussian noise model with mean value $\eta$ and with standard deviation $\delta$. We construct in this way a suite of 1000 mock catalogs which are tessellated with HEALPix and Fourier transformed in exactly the same way as the data.

The systematic errors that affect our analysis, defined as the difference between the input parameter and the average value inferred by means of the Monte Carlo simulations, are always smaller than the statistical error. However, they are non-negligible and we thus correct the observational measurements for these bias factors.

## 4. Data

### 4.1 The Pantheon sample

The Pantheon SNIa compilation [9] is comprised of 1048 objects lying in the interval $0.01 < z < 2.26$. The catalog was assembled using data from the Supernova Legacy Survey (SNLS) [10], the Sloan Digital Sky Survey (SDSS) [11, 12], Pan-STARS1 (PS1) [9], [13–17] the Carnegie Supernova Project (CSP) [18] and various surveys made possible by the Hubble Space Telescope (HST), namely CANDLES/ CLASH [19–21], GOODS [22] and SCP [23].

In Fig 1 (the first column) the angular distribution of the Pantheon data is shown together with the differential number counts profile $dN(z)$ as a function of redshift. There are no objects in the

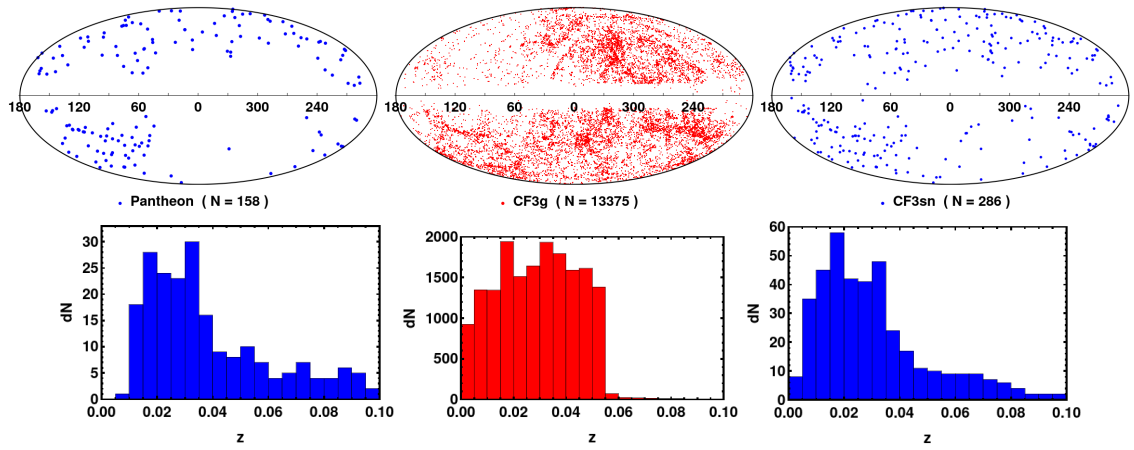


**Figure 1:** *Upper left :* Mollweide projection, in galactic coordinates, of the distribution of the Pantheon SNIa with redshift $0.01 < z < 0.05$. *Lower left :* histograms of the number of counts as a function of redshift. The second and the third columns are the same as the first, but for the CF3g and CF3sn samples respectively.

very local patch of the universe, below $z = 0.01$, and the sample becomes quickly anisotropic as soon as the redshift is larger than $z = 0.05$. It also becomes in-homogthaneneous, i.e. the scaling of $dN$ is not anymore proportional to $z^2$, for $z \gtrsim 0.04$. As a consequence, to minimize possible biases and systematic effects, a trade-off threshold value $z = 0.05$ is chosen for selecting the SNIa sample to be used in this study. This leaves us with a subsample containing 158 SNIa.

### 4.2 The Cosmicflows-3 data

For the purposes of our analysis, we complement the Pantheon supernovae sample with the Cosmicflows-3 catalog [24]. This is an all-sky galaxy catalog comprised of 17669 nearby galaxies $z \leq 0.116$ for which redshift-independent distances are inferred using the the correlation between galaxy rotation and luminosity (Tully-Fisher law), or the Fundamental Plane methods.

The angular and radial distribution of the Cosmicflows-3 galaxies is shown in Fig. 1 (the second and the third columns). They are fairly evenly distributed in both redshift and position in the sky except for redshifts greater than 0.05. So, we don't include the galaxies beyond this redshift since the sample becomes too sparse and covers the sky anisotropically. We also exclude from the sample, galaxies with redshift less than 0.01, in order to facilitate the comparison with the results obtained from the Pantheon data. We, therefore, focus our analysis on the Cosmicflows-3 subsample which is constrained in the range $0.01 < z < 0.05$ and includes 13661 galaxies.

Within this redshift range, the CF3 catalog contains 286 galaxies hosting a SNIa (Fig. 1 third column) for which the distance modulus is known using the standard candle method. Although systematically homogenized, this compilation of SNIa-based distances remains fundamentally heterogeneous, with distance moduli derived from different light curve fitters. Although this dataset contains the Pantheon as a subsample, we use it as a control sample to check the robustness of the results we obtain using the Pantheon dataset alone. In what follows, we will refer to the CF3 subsample with SNIa-based distances as CF3sn and indicate the complementary set with the acronym CF3g.

| Sample | $N_{pix}$ | $l_d$ | $b_d$ | $\hat{C}_1$ ($10^{-4}$) | $\Delta\eta_1$ ($10^{-2}$) | p-value (%) | $l_q$ | $b_q$ | $\hat{C}_2$ ($10^{-4}$) | $\Delta\eta_2$ ($10^{-2}$) | p-value (%) | $l_t$ | $b_t$ | $\hat{C}_3$ ($10^{-4}$) | $\Delta\eta_3$ ($10^{-2}$) | p-value (%) |
|---|---|---|---|---|---|---|---|---|---|---|---|---|---|---|---|---|
| CF3 [0.01, 0.05] | 192 | $291 \pm 15$ | $12 \pm 7$ | $3.0 \pm 1.6$ | 1.6 | 0.03 | $323 \pm 16$ | $9 \pm 4$ | $2.4 \pm 0.9$ | 1.9 | 0.12 | $289 \pm 24$ | $16 \pm 15$ | $0.1 \pm 0.4$ | 1.2 | 30.44 |
| CF3 [0.01, 0.05] | 48 | $283 \pm 6$ | $12 \pm 5$ | $5.3 \pm 0.8$ | 1.9 | $< 0.01$ | $310 \pm 11$ | $4 \pm 8$ | $0.9 \pm 0.3$ | 1.1 | $< 0.01$ | $284 \pm 7$ | $12 \pm 5$ | $0.5 \pm 0.2$ | 1.3 | 0.01 |
| CF3g [0.01, 0.05] | 48 | $286 \pm 7$ | $4 \pm 6$ | $7.0 \pm 1.0$ | 2.0 | $< 0.01$ | $338 \pm 8$ | $22 \pm 5$ | $1.1 \pm 0.4$ | 1.3 | $< 0.01$ | $255 \pm 9$ | $11 \pm 5$ | $0.7 \pm 0.2$ | 1.5 | 0.01 |
| CF3 [0.01, 0.05] | 12 | $285 \pm 5$ | $11 \pm 4$ | $5.1 \pm 0.8$ | 1.9 | $< 0.01$ | $308 \pm 7$ | $1 \pm 7$ | $1 \pm 0.3$ | 1.1 | $< 0.01$ | - | - | - | - | - |
| CF3g [0.01, 0.05] | 12 | $296 \pm 6$ | $18 \pm 5$ | $4.0 \pm 0.6$ | 1.7 | $< 0.01$ | $323 \pm 34$ | $2 \pm 17$ | $1.3 \pm 0.4$ | 1.4 | $< 0.01$ | - | - | - | - | - |
| CF3sn [0.01, 0.05] | 12 | $322 \pm 23$ | $-8 \pm 18$ | $3.7 \pm 1.5$ | 1.5 | 0.27 | $343 \pm 15$ | $-8 \pm 10$ | $1.7 \pm 1.4$ | 1.7 | 2.90 | - | - | - | - | - |
| Pantheon [0.01, 0.05] | 12 | $334 \pm 42$ | $6 \pm 20$ | $3.5 \pm 2.7$ | 1.6 | 4.37 | 337 | $-5$ | $0.6 \pm 1.9$ | 1.6 | 33.33 | - | - | - | - | - |
| CF3 [0.01, 0.03] | 12 | $279 \pm 5$ | $12 \pm 5$ | $7.8 \pm 1.0$ | 2.3 | $< 0.01$ | $310 \pm 8$ | $11 \pm 6$ | $2.9 \pm 0.6$ | 1.9 | $< 0.01$ | - | - | - | - | - |
| CF3 [0.03, 0.05] | 12 | $301 \pm 15$ | $10 \pm 14$ | $1.1 \pm 0.7$ | 1.0 | 0.03 | $277 \pm 28$ | $-12 \pm 11$ | $0.9 \pm 0.3$ | 1.0 | 2.04 | - | - | - | - | - |

**Table 1:** Parameters of the spherical harmonic decomposition. Central values are not the bare value returned by the spherical harmonic estimator but are obtained after subtracting systematic effect determined by means of 1000 Monte Carlo simulations. We quote also the direction for the dipole, and direction of the peaks of the $\ell = 2$ and 3 multipoles which are close to the direction of the dipole, and also the amplitude $\Delta\eta_l = \frac{\eta_{2max} - |\eta_{2min}|}{2}$. The p-value is computed by using 10000 Monte Carlo simulations. For Pantheon, the error in the direction of the quadrupole is not quoted because it is larger the 180 degrees.

## 5. Results

In this section, we present and comment on the results obtained by applying the formalism to various datasets. The relevant parameters of the SH analysis of the expansion rate field are quoted in TABLE 1. FIG. 2 shows the $\eta$ field for the CF3 sample tessellated according to different resolutions (192, 48 and 12 pixels). Smoothing mostly impact the errors with which the relevant SH parameters are estimated, with generally smaller error as the number of pixels decreases. The central values of the SH parameter, instead, are statistically stable: they fluctuate from one reconstruction to the next, but the discrepancies are within what is expected from a random sampling of a common underlying Gaussian distribution. The results are thus globally independent of the pixelization strategy adopted. For SNIa, because the number of objects is smaller, we can only use the lowest resolution (12 pixels) to do the multipole expansion. The price to pay is that now the higher multipoles ($\ell \geq 3$) cannot be estimated.

We then ask whether each multipole found in each data sample is statistically significant. So, we perform Monte Carlo simulations to find the $p$-value, which is the probability to find amplitude of each multipole equal to or higher than the measured value, if we consider a model of the expansion rate fluctuation $\eta$ that contains only the monopole and no higher order terms and generate 10000 Monte Carlo mock catalogs simulating each data set. This is done by replacing the model distances with a fictitious one randomly drawn from a Gaussian distribution $G(\eta, \delta)$.

The strongest contribution to the signal is provided by the dipole term, whose maximal intensity is about 1% of the signal locked in the normalizing term $\log H_0$, i.e. $\sim 4.5\%$ of $H_0$. The power locked in the dipole (as determined using the the CF3g sample) is $\hat{C}_1 = (4.0 \pm 0.6) \cdot 10^{-4}$, an estimation characterised by a high signal-to-noise ratio (snr $\sim 6.6$). Consistently, this value is in excellent agreement (well within $1\sigma$) with that estimated from both the CF3sn and the Pantheon

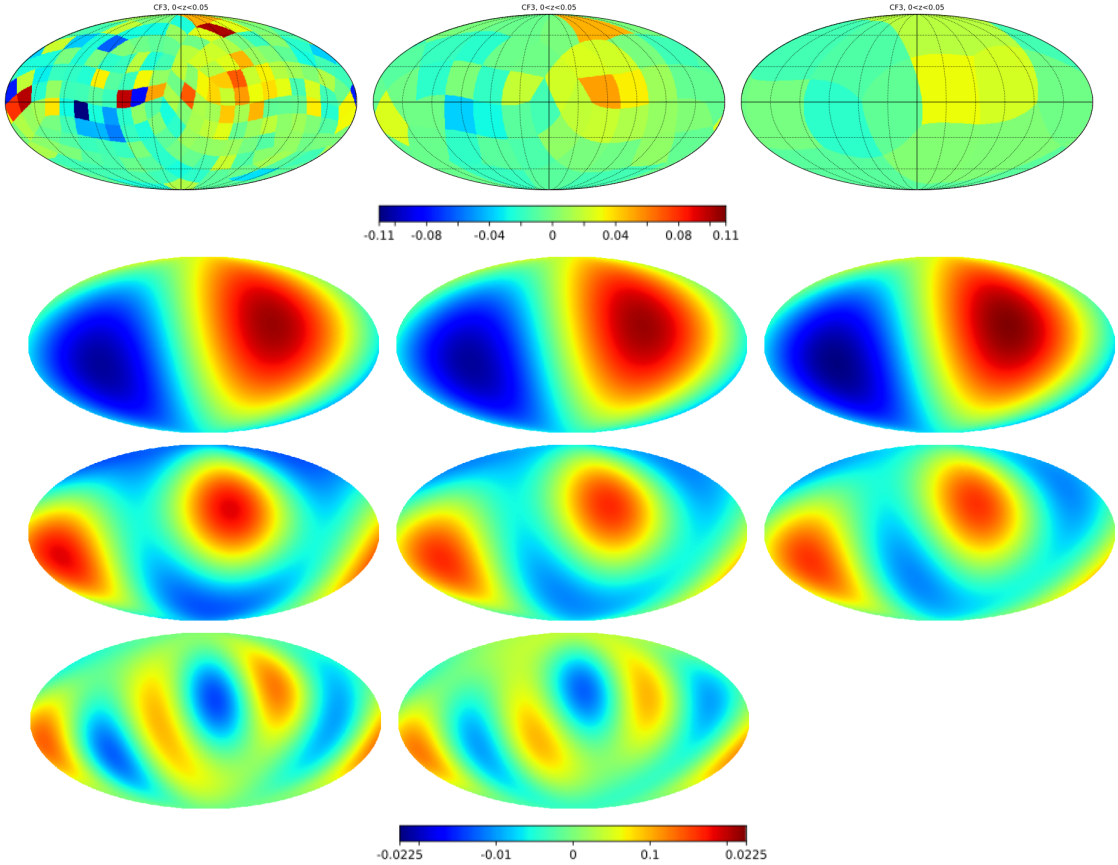


**Figure 2:** *Upper panel:* the angular $\eta$ field traced by the CF3. From left to right are shown different resolution maps corresponding to the tessellation of the sky with 192, 48 and 12 HEALPix cells. The dipole $\eta_1$ (second panel from the top), quadrupole $\eta_2$ (third panel from the top), and octupole $\eta_3$ (bottom panel) components are also shown.

sample ( $(3.7 \pm 1.5) \cdot 10^{-4}$ and $(3.5 \pm 2.7) \cdot 10^{-4}$ respectively).

We find that the contribution of the quadrupole component to the anisotropies observed in the $\eta$ expansion field is significant both in terms of its amplitude, which is comparable to that of the dipole ( $max(\eta_2) \sim max(\eta_1)$), and in terms of its statistical significance (measured by the signal-to-noise ratio ($snr \sim 3.25$ for CF3g and $snr \sim 1.2$ for CF3sn)

More intriguingly we find that the maximum of the quadrupole signal is aligned with the dipole direction (see FIG. 2). This peculiar alignment is consistently and independently confirmed by both galaxy (CF3g) and SNIa (CF3sn) samples (see TABLE 1 and FIG. 3). We highlight the fact that inferences made with the different samples are consistent, but there is one difference that deserves attention and further investigation: there is no evidence of a quadrupole component in the Pantheon data as judged from the amplitude of the $\hat{C}_2$ power, both in term of its $snr$ and of its $p$-value.

Interestingly, we find evidence ($snr \sim 2.5$) that the contribution of the octupole is also not negligible, at least when the whole CF3 sample is analyzed with a 48 HEALPix pixel smoothing. The power stocked in this component is roughly half that in the quadrupole although the intensity peaks at a value comparable to the maximum intensity of the quadrupole. Even more unexpected

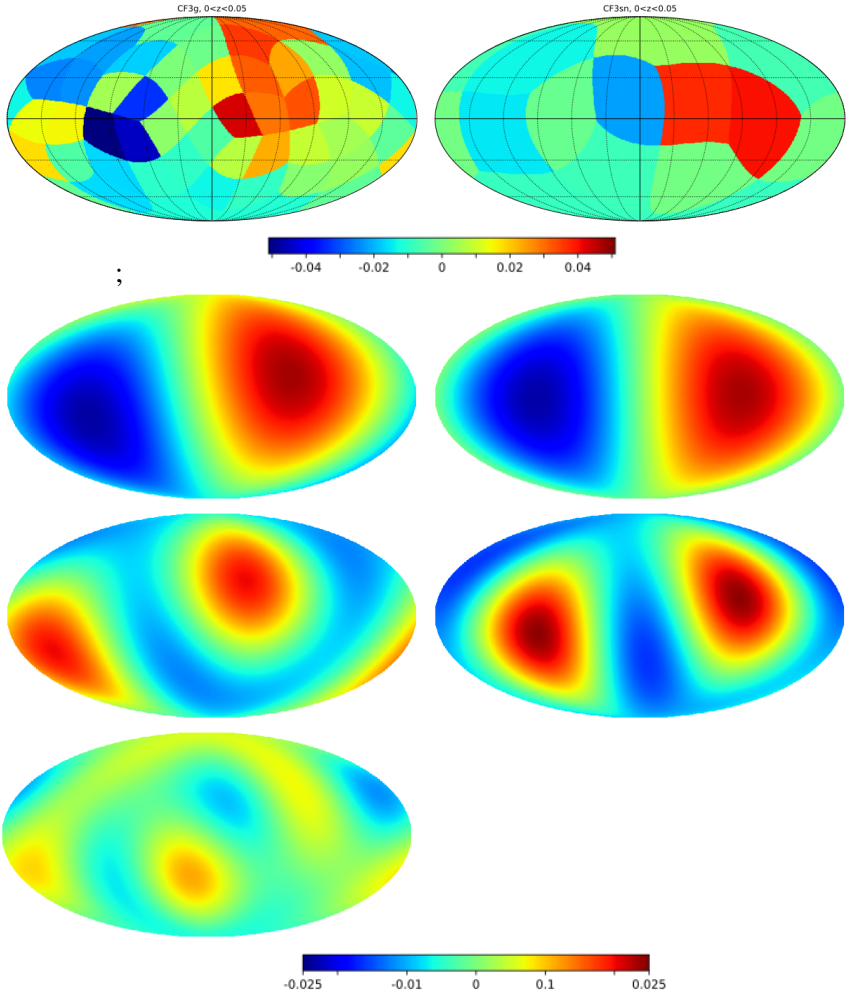


**Figure 3:** *Left panel:* the $\eta$ field tessellated into 48 pixels and traced by the CF3g sample. The dipole $\eta_1$ (second panel from the top), quadrupole $\eta_2$ (third panel from the top), and octupole $\eta_3$ (bottom panel) components are also shown. *Right panel:* same as above, but now the expansion rate fluctuation field is tessellated into 12 pixels and traced by the CF3sn sample.

is the fact that the direction of the maximum of the octupole component ($l_t = 284 \pm 7, b_t = 12 \pm 5$) appears to be aligned with that of the dipole ($l_d = 283 \pm 6, b_d = 12 \pm 5$) and of the quadrupole ($l_q = 310 \pm 11, b_q = 4 \pm 8$) (see TABLE 1).

It is however critical to assess whether their curious structure is the result of a fortuitous averaging coincidence. To investigate this issue we repeat the analysis separately in two redshift intervals $0.01 \leq z \leq 0.03$ and $0.03 \leq z \leq 0.5$. These are the smallest subvolumes that still provide detections with acceptable *snr* and low risk of misinterpretation (low p-value), if only for the CF3 sample. Results are shown in Fig. 4.

The direction of the dipole and the quadrupole reconstructed in the two volumes consistently point in the same direction (to within about $1\sigma$) and is also in excellent agreement with the results found for the whole samples. This confirms that the alignment phenomenon is not a random overlap but rather physical in nature. There is, instead a significant change in the power spectrum amplitude

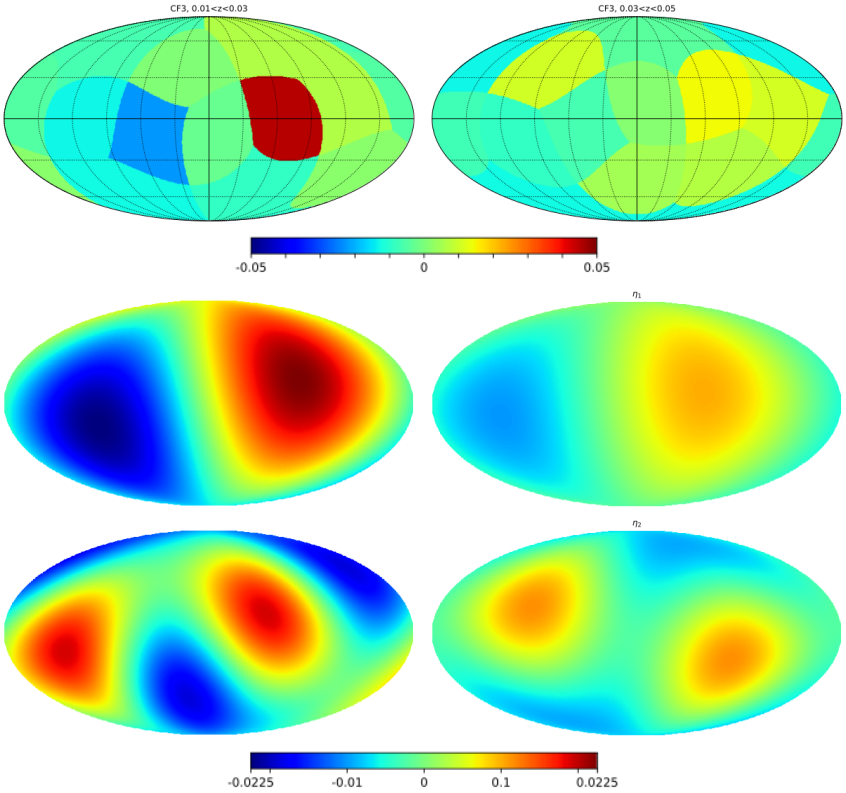


**Figure 4:** *Left panels:* The $\eta$ field (upper), its dipolar (center) and quadrupolar (lower) components traced by the CF3 sample in the redshift interval $0.01 \leq z \leq 0.03$. *Right panels* The same as before but for galaxies in the deeper redshift range $0.03 \leq z \leq 0.05$.

of the multipoles. The $\hat{C}_1$ component decreases by more than about $5.5\sigma$ as the redshift of the sample doubles. The same decrement with depth ($\sim 3\sigma$) is observed for the amplitude of the $\hat{C}_2$ coefficient.

### 5.1 Axial symmetry of the multipoles

In FIG. 5 we show the 3D structure of the quadrupole component of the expansion rate fluctuations $\eta$ reconstructed using either the galaxy or the supernovae sample. This figure offers a different perspective on the dipole-quadrupole alignment. It shows that both quadrupoles independently reconstructed using galaxy and supernova data present an axially symmetric configuration which strongly polarizes in the direction defined by the dipole.

This additional symmetry, although physically unexpected since it seems to imply extreme fine-tuning in the local distribution of matter fluctuations, makes it possible to simplify, at least mathematically, the analysis of the anisotropies of the eta field. The fact that the direction $(l_d, b_d)$ along which the multipoles aligne (Apex direction) defines not only a preferred axis, but indeed an axis of symmetry implies that the expansion rate fluctuation field $\eta$ effectively depends only on a single variable, the polar angle $\alpha$ between the line-of-sight of an object and the direction $(l_d, b_d)$. A simple expansion of the field in Legendre polynomials $P_\ell(\cos\alpha)$, as opposed to the full spherical harmonics machinery, is thus enough for seizing the essential functional behavior of the $\eta$ field.

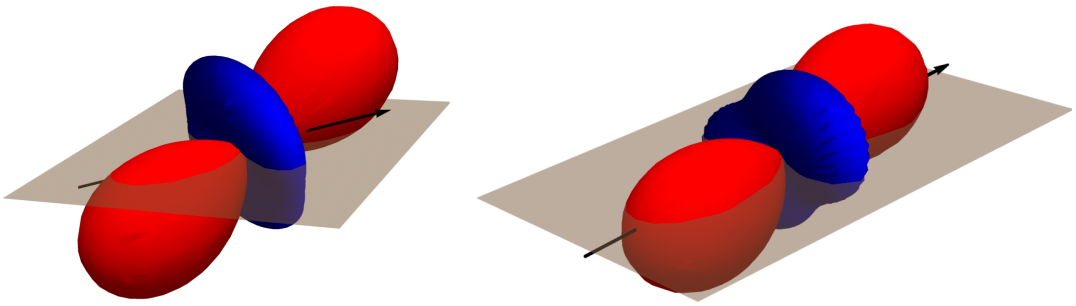

**Figure 5:** The 3D structure of the multipole component $\eta_2$ of the CF3g sample (left panel) and for the CF3sn sample (right panel). The radial coordinate represents the absolute value for $\eta$; the red and blue colors indicate positive and negative signs respectively. For reference, the gray surface represents the orientation of the galactic plane while the black arrow gives the direction of the dipole as reconstructed for each sample.

| Sample | $a_1$ $(10^{-2})$ | $a_2$ $(10^{-2})$ | $a_3$ $(10^{-2})$ | $\chi^2_1/dof$ | $\chi^2_2/dof$ | $\chi^2_3/dof$ | $v_b$ (km/s) |
|---|---|---|---|---|---|---|---|
| CF3 $0.01 < z < 0.05$ | $1.7 \pm 0.1$ | $0.9 \pm 0.2$ | $0.6 \pm 0.2$ | 8.50 | 4.83 | 2.71 | $292 \pm 21$ |
| CF3g $0.01 < z < 0.05$ | $1.8 \pm 0.1$ | $0.9 \pm 0.2$ | $0.5 \pm 0.2$ | 7.59 | 4.34 | 2.83 | $307 \pm 23$ |
| CF3sn $0.01 < z < 0.05$ | $1.3 \pm 0.4$ | $0.5 \pm 0.5$ | $0.4 \pm 0.5$ | 1.53 | 1.40 | 1.18 | $195 \pm 57$ |
| Pantheon $0.01 < z < 0.05$ | $1.6 \pm 0.7$ | $0.1 \pm 0.7$ | $-0.8 \pm 0.5$ | 0.46 | 0.46 | 0.54 | $243 \pm 110$ |

**Table 2:** The coefficient of Legendre expansion for 10 bins in $\cos\alpha$ where $\alpha$ is the angle between the and principal axis $(l, b) = (285, 11)$. The error is calculated by the error of average $\eta$ for each bin. $a_\ell$ is calculated by eq. (10).

The average value $\eta(\alpha)$ reconstructed in open circular sectors of identical width having the center on the axis of symmetry and angular separation $\alpha$ from the apex direction is shown in FIG 6 for the galaxy and SNIa samples. The Fourier coefficients of the expansion

$$\eta(\alpha) = \sum_{\ell=1}^{3} a_\ell P_\ell(\cos\alpha), \tag{9}$$

are computed as

$$a_\ell = \frac{2\ell+1}{N_{bins}} \sum_{i=1}^{N_{bins}} \eta(\cos\alpha_i) P_\ell(\cos\alpha_i), \tag{10}$$

and the results are quoted in TABLE 2.

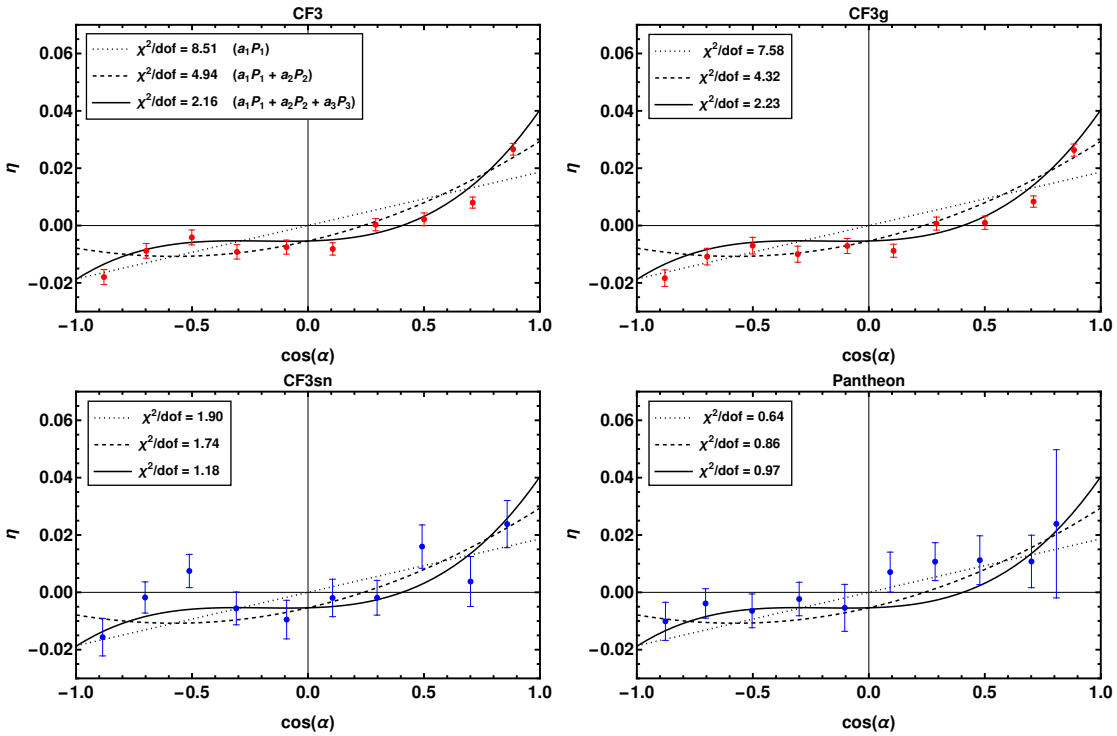


**Figure 6:** *Upper left:* average value of $\eta$, for the CF3 sample, in open spherical sectors of identical width $\Delta \cos\alpha = 0.2$ and angular separation $\alpha$ from the direction $l = 285, b = 11$. The dotted line corresponds to the dipolar model ( $a_1 = 1.9 \cdot 10^{-2}$), the dashed line includes also the contribution of a quadrupole term ( $a_2 = 1.1 \cdot 10^{-2}$). The effects of adding the octupole term ( $a_3 = 1.1 \cdot 10^{-2}$) are shown by the solid line. These models are compared to CF3g data (*upper right*), the CF3sn data (*lower right*) and the Pantheon data (*lower right*). In this latter case, Note the absence of data in the rightmost bin, i.e., along the direction in which the low-order multipoles of the CF3 sample align.

### 5.2 Bulk motion model

The perturbation theory of the standard cosmological model provides a framework for interpreting our results. If peculiar velocity are random and uncorrelated in a given angular direction, the average expansion field $\eta$ vanishes in that direction. Consider instead a peculiar velocity field $v_b$ which is constant in both direction and amplitude over a typical scale $R$. If we choose $\alpha$ as measuring the angle between its direction and the line of sight, the expansion field is predicted to vary as (cf. eq. 3)

$$\eta(\alpha) = \frac{v_b}{\ln 10} \langle (1+z)/z \rangle \cos\alpha. \tag{11}$$

Suppose that $\langle (1+z)/z \rangle$, the average over the volume subtended by circular bands of angular separation $\alpha$ from the direction of the bulk motion, does not depend on $\alpha$, which is a fairly good approximation for large samples. Then, by comparing (11) with (9), we deduce that the bi-dimensional expansion field $\eta$ is compatible with being the sky projected realisation of a three-dimensional bulk flow model. The amplitude of the bulk velocity follows from the amplitude of the

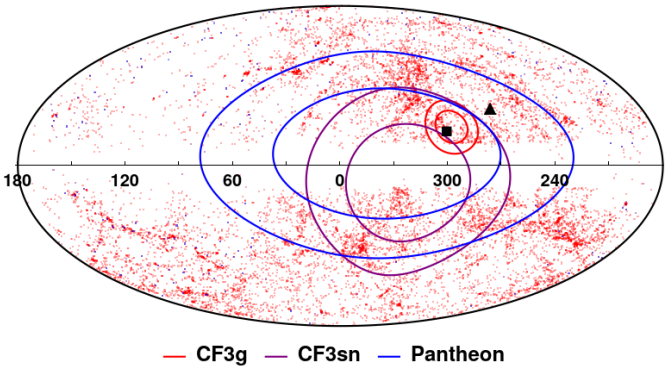


**Figure 7:** Likelihood contours ($1\sigma$ and $2\sigma$) for the direction of the dipole reconstructed using 12 pixels for the CF3g (red lines), CF3sn (purple lines) and Pantheon (blue lines) samples. For reference, the direction of the motion of the barycenter of the Local Group with respect to the CMB $(l, b) \approx (270, 27)$ [25] is marked (black triangle) together with the direction of its bulk component $(l, b) \approx (299, 15)$ (Black square).

dipolar parameter $a_1$ (the coefficient of the expansion on the Legendre basis $P_1$)

$$v_b = \frac{a_1 \ln 10}{\langle (1+z)/z \rangle}. \tag{12}$$

Assuming 500 km/s as a typical value for the peculiar velocity of galaxies, we expect the latter relation to apply fairly well for objects with $z \geq 0.01$, those considered in our analysis. Note that in this picture, the amplitude of the bulk is controlled by the amplitude of the dipolar parameter $a_1$ and also by the depth of the survey volume.

The direction of the bulk motion for the three samples is shown in Figure 7. This direction results from separating in the SH analysis the direction of the dipole from that of other higher order multipoles. However, due to the alignment of the lower multipoles, the direction of the bulk coincides fairly well with the direction of maximum anisotropy in the $\eta$ maps.

### 5.3 Effects of anisotropies on the Hubble diagram

As a consequence of the alignment of the maximal intensities of its dipole, quadrupole and octupole components, the expansion field displays an 'apex' towards which the rate of expansion is significantly higher than average and an anti-apex where the expansions is coherently lower than the monopole component. This preferred axis characteristically shows up in the Hubble diagram.

FIG. 8 shows the difference between the best estimates of $H_0$ deduced from the Hubble diagram analysis of the Pantheon SNIa dataset in two antipodal directions. In practice this is achieved by fitting the relation $\mu = 5\log(z/H_0) + 25$ separately to the distance modulus of the Pantheon objects falling in two cones of total width 120° (about 25% of the sky) centered on the observer and whose axes point in antipodal directions (apex and antiapex).

The left panel in FIG. 8 is obtained without implementing any redshift correction. As a result we find that Hubble constant estimates may show variation as high as $\Delta H_0 = (4.1 \pm 1.1)$ km/s/Mpc between antipodal directions along the dipole axis. In the the second panel we replace $z$ with $z_h$ in the distance modulus formula, i.e. we correct the redshift for the peculiar velocity of the objects

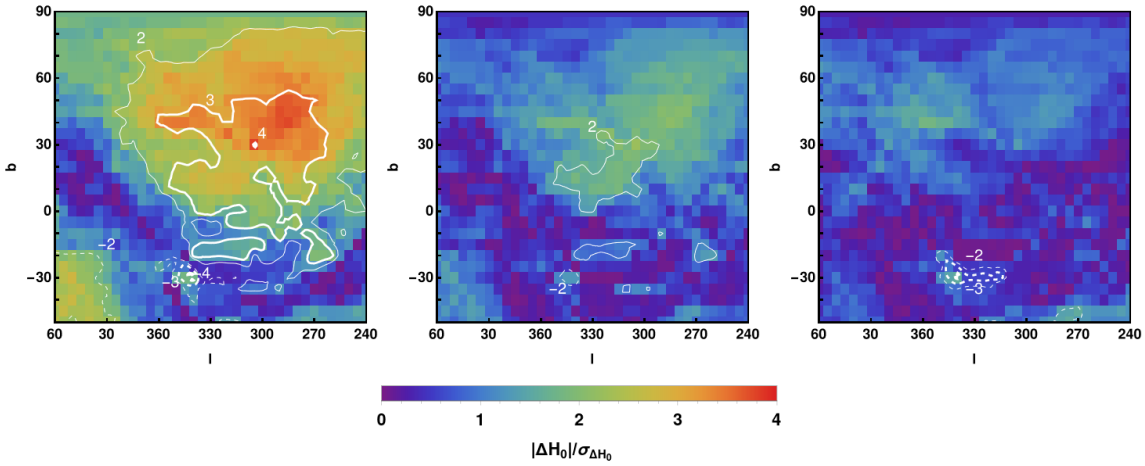


**Figure 8:** *left panel:* Solid and dashed lines represent positive and negative isocontours of $\Delta H_0 = H^{apex} - H_0^{antiapex}$ calculated using Pantheon SNe with angular separation $\leq 60^\circ$ from an axis of coordinates $(l, b)$. Different thicknesses correspond to different amplitudes, as indicated by the labels. Isocontours are superimposed to the smoothed signal-to-noise map. *Central panel:* as above, but after subtracting from the redshift of each object the peculiar velocities listed in the Pantheon catalog. *Right panel:* as above, but after correcting the redshift using the $\eta(\alpha)$ model (9) with Fourier coefficients computed from the CF3g data (and quoted in the second row of TABLE 2). The maximum antipodal anisotropy detected are $(l, b, \Delta H_0) = (305, 30, 4.1 \pm 1.1), (305, 30, 2.4 \pm 1.1)$ and $(360, 40, 1.9 \pm 0.9)$ respectively.

as done by the compilers of the Pantheon sample, i.e. by using the model of [26](we refer to this redshift as to the *Hubble diagram redshift*). In the third panel we show the Hubble constant obtained by fitting data after correcting the distance modulus to subtract the expansion rate fluctuations $\eta$, i.e. by means of the formula

$$\mu = 5 \log \left( \frac{z}{H_0} \right) + 25 - 5\eta. \tag{13}$$

Here $\eta$ is approximated using the Legendre expansion (9) with Fourier coefficients computed from an independentdata sample, the iCF3g galaxy data. These coefficients are quoted in the second row of TABLE 2. As we can see in FIG. 8, correcting for anisotropic motions using the Hubble diagram redshift reduces the amplitude of the dipolar anisotropy in both amplitude and signal to noise ratio. Indeed, the systematic difference in $H_0$ measurements in antipolar directions is reduced to $\Delta H_0 = (2.4 \pm 1.1)$ km/s/Mpc once model-dependent correction for peculiar velocity flows are implemented. However the residuals still show the presence of an anisotropic signal with a non-trivial dipolar structure which is incompatible with being a residual fluctuation of random nature. A better subtraction of peculiar motion effects is achieved by implementing the $\eta$ correction scheme, as can be seen in the right panel of FIG. 8. In this latter case, the distribution of residual fluctuations $\Delta H_0$ has not only an amplitude which effectively vanishes, but is also consistently centered on zero, no dipole structure being present anymore. As a result, the value of the best fitting $H_0$ is systematically revised upwards by nearly 0.7 km/s/Mpc (about $2\sigma$) compared to the value deduced from the Hubble diagram using the uncorrected observed redshift. The goodness of fit is also improved.

## 6. Conclusion

We have designed an observable that captures, in a statistically unbiased way, the average angular fluctuations in the local expansion rate. This quantity allows to characterize anisotropies as well as non-linearities in the redshift-distance relation in a model-independent way.

We have estimated the $\eta$ field using catalogs of redshift-independent distances such as the Cosmicflows-3 galaxy sample and the Pantheon sample of supernovae. We have then compressed the resulting signal into independent spherical harmonics components to better analyse the structure of the anisotropies in the redshift-distance relation.

All data samples analyzed consistently suggest the existence of a preferred axis in the local universe ($0.01 < z < 0.05$), in the direction $(l, b) = (285 \pm 5, 11 \pm 4)$, along which the local redshift-distance relation displays a dipolar pattern, and this is mainly related to the average peculiar velocity $v_b = (299 \pm 22)$ km/s in that direction.

Interestingly, the SH analysis suggests that a simple dipole provides a poor representation of the angular fluctuations in the local expansion rate. We find, that about 50% of the anisotropic signal is contributed by a quadrupole component. This is independently confirmed by the CF3g and CF3sn samples, which also consistently show that the axis of the maximum of the quadrupole is aligned with the direction of the dipole. This intriguing feature persists when the sample is split in two and the analysis is repeated in two separate spherical shells of different depths. The analyses of both samples also agree on the shape of the quadrupole. It is a rather axisymmetrical configuration, with no indication of prominent secondary axes. Furthermore, we find a relatively large signal for the octupole at least for the CF3 sample of galaxies. Its configuration is also quite peculiar, with its axis of maximal intensity colinear with the axes of the dipole and the quadrupole.

After factoring out from the Pantheon sample the contribution of these peculiar velocities (reconstructed by applying prescriptions of the theory of linear perturbations to the observed fluctuations in the spatial distribution of galaxies), we observe that the $H_0$ perturbations, although reduced in amplitude, do not distribute as random (Gaussian) residuals. Curiously, the structure of the expansion rate field still presents an axial anisotropy in the same general direction as the CMB dipole.

In this regard, we show how to exploit the expansion rate fluctuation field $\eta$ to subtract redshift anisotropies. In practice, we correct the distance moduli of the Pantheon sample with a neat three-parameter formula (see eq. (9)) calibrated using the independent sample CF3g. Despite its simplicity, the approach is efficient to remove the anisotropy of the redshift-distance relation for Pantheon sample.

To conclude, a key objective has been to show, as a proof-of-concept, the potential power of a new observable, the expansion rate fluctuation $\eta$, both to study the structure of the anisotropies in the redshift-distance relation and to minimize eventual systematics in the locally inferred value of $H_0$. It is thus necessary, in follow-up papers, to build on the current formalism by doing a more intensive data analysis. This will include the use of updated and expanded data sets, including Cosmicflows-4 [27], Pantheon+ [28]. The longterm goal is to asses whether and which proposal for a non-standard metric faithfully describes the multipolar anisotropy pattern detected in our analysis.

## References


[1] E. Di Valentino, O. Mena, S. Pan, L. Visinelli, W. Yang, A. Melchiorri et al., *In the realm of the hubble tension—a review of solutions **, *Classical and Quantum Gravity* **38** (2021) 153001.

[2] B. Kalbouneh, C. Marinoni and J. Bel, *Multipole expansion of the local expansion rate*, *Physical Review D* **107** (2023) .

[3] Planck collaboration, *Planck 2018 results. I. Overview and the cosmological legacy of Planck*, *Astron. Astrophys.* **641** (2020) A1 [1807.06205].

[4] C. Clarkson and R. Maartens, *Inhomogeneity and the foundations of concordance cosmology*, *Class. Quant. Grav.* **27** (2010) 124008 [1005.2165].

[5] J. Kristian and R.K. Sachs, *Observations in Cosmology*, **143** (1966) 379.

[6] A. Heinesen, *Multipole decomposition of the general luminosity distance hubble law — a new framework for observational cosmology*, *Journal of Cosmology and Astroparticle Physics* **2021** (2021) 008.

[7] B. Kalbouneh and C. Marinoni, *The multipolar structure of the local universe: effects induced by the choice of observers and distance reconstruction schemes*, *In prep.* (2023) .

[8] K.M. Górski, E. Hivon, A.J. Banday, B.D. Wandelt, F.K. Hansen, M. Reinecke et al., *HEALPix - A Framework for high resolution discretization, and fast analysis of data distributed on the sphere*, *Astrophys. J.* **622** (2005) 759 [astro-ph/0409513].

[9] D.M. Scolnic, D.O. Jones, A. Rest, Y.C. Pan, R. Chornock, R.J. Foley et al., *The Complete Light-curve Sample of Spectroscopically Confirmed SNe Ia from Pan-STARRS1 and Cosmological Constraints from the Combined Pantheon Sample*, **859** (2018) 101 [1710.00845].

[10] J. Guy, M. Sullivan, A. Conley, N. Regnault, P. Astier, C. Balland et al., *The Supernova Legacy Survey 3-year sample: Type Ia supernovae photometric distances and cosmological constraints*, **523** (2010) A7 [1010.4743].

[11] M. Smith, R.C. Nichol, B. Dilday, J. Marriner, R. Kessler, B. Bassett et al., *The SDSS-II Supernova Survey: Parameterizing the Type Ia Supernova Rate as a Function of Host Galaxy Properties*, **755** (2012) 61 [1108.4923].

[12] SDSS collaboration, *The Data Release of the Sloan Digital Sky Survey-II Supernova Survey*, *Publ. Astron. Soc. Pac.* **130** (2018) 064002 [1401.3317].

[13] A.G. Riess, R.P. Kirshner, B.P. Schmidt, S. Jha, P. Challis, P.M. Garnavich et al., *BVRI Light Curves for 22 Type IA Supernovae*, **117** (1999) 707 [astro-ph/9810291].

[14] S. Jha, R.P. Kirshner, P. Challis, P.M. Garnavich, T. Matheson, A.M. Soderberg et al., *UBVRI Light Curves of 44 Type Ia Supernovae*, **131** (2006) 527 [astro-ph/0509234].

[15] M. Hicken, W.M. Wood-Vasey, S. Blondin, P. Challis, S. Jha, P.L. Kelly et al., *Improved Dark Energy Constraints from ~100 New CfA Supernova Type Ia Light Curves*, **700** (2009) 1097 [0901.4804].

[16] M. Hicken, P. Challis, S. Jha, R.P. Kirshner, T. Matheson, M. Modjaz et al., *CfA3: 185 Type Ia Supernova Light Curves from the CfA*, **700** (2009) 331 [0901.4787].

[17] M. Hicken, P. Challis, R.P. Kirshner, A. Rest, C.E. Cramer, W.M. Wood-Vasey et al., *CfA4: Light Curves for 94 Type Ia Supernovae*, **200** (2012) 12 [1205.4493].

[18] C. Contreras, M. Hamuy, M.M. Phillips, G. Folatelli, N.B. Suntzeff, S.E. Persson et al., *The Carnegie Supernova Project: First Photometry Data Release of Low-Redshift Type Ia Supernovae*, **139** (2010) 519 [0910.3330].

[19] S.A. Rodney, A.G. Riess, L.-G. Strolger, T. Dahlen, O. Graur, S. Casertano et al., *Type Ia Supernova Rate Measurements to Redshift 2.5 from CANDELS: Searching for Prompt Explosions in the Early Universe*, **148** (2014) 13 [1401.7978].

[20] O. Graur, S.A. Rodney, D. Maoz, A.G. Riess, S.W. Jha, M. Postman et al., *Type-Ia Supernova Rates to Redshift 2.4 from CLASH: The Cluster Lensing And Supernova Survey with Hubble*, **783** (2014) 28 [1310.3495].

[21] A.G. Riess, S.A. Rodney, D.M. Scolnic, D.L. Shafer, L.-G. Strolger, H.C. Ferguson et al., *Type Ia Supernova Distances at Redshift >1.5 from the Hubble Space Telescope Multi-cycle Treasury Programs: The Early Expansion Rate*, **853** (2018) 126 [1710.00844].

[22] A.G. Riess, L.-G. Strolger, S. Casertano, H.C. Ferguson, B. Mobasher, B. Gold et al., *New Hubble Space Telescope Discoveries of Type Ia Supernovae at z >= 1: Narrowing Constraints on the Early Behavior of Dark Energy*, **659** (2007) 98 [astro-ph/0611572].

[23] N. Suzuki, D. Rubin, C. Lidman, G. Aldering, R. Amanullah, K. Barbary et al., *The Hubble Space Telescope Cluster Supernova Survey. V. Improving the Dark-energy Constraints above z > 1 and Building an Early-type-hosted Supernova Sample*, **746** (2012) 85 [1105.3470].

[24] R.B. Tully, H.M. Courtois and J.G. Sorce, *COSMICFLOWS-3*, *The Astronomical Journal* **152** (2016) 50.

[25] D.J. Fixsen, E.S. Cheng, J.M. Gales, J.C. Mather, R.A. Shafer and E.L. Wright, *The Cosmic Microwave Background spectrum from the full COBE FIRAS data set*, *Astrophys. J.* **473** (1996) 576 [astro-ph/9605054].

[26] J. Carrick, S.J. Turnbull, G. Lavaux and M.J. Hudson, *Cosmological parameters from the comparison of peculiar velocities with predictions from the 2m density field*, *Monthly Notices of the Royal Astronomical Society* **450** (2015) 317.

[27] E. Kourkchi, R.B. Tully, S. Eftekharzadeh, J. Llop, H.M. Courtois, D. Guinet et al., *Cosmicflows-4: The Catalog of ~10,000 Tully-Fisher Distances*, **902** (2020) 145 [2009.00733].

[28] A.G. Riess et al., *A Comprehensive Measurement of the Local Value of the Hubble Constant with 1 km $s^1$ $Mpc^1$ Uncertainty from the Hubble Space Telescope and the SH0ES Team*, *Astrophys. J. Lett.* **934** (2022) L7 [2112.04510].